Accepted Manuscript

Title: Structural Thermal Stability of Graphene Oxide-doped Copper-cobalt Oxide Coatings as a Solar Selective Surface

Author: M. Mahbubur Rahman, Zhong-Tao Jiang, Chun-Yang Yin, Lee Siang Chuah, Hooi-Ling Lee, Amun Amri, Bee-Min Goh, Barry J. Wood, Chris Creagh, Nicholas Mondinos, Mohmmednoor Altarawneh, Bogdan Z. Dlugogorski

PII: S1005-0302(16)30154-2
DOI: http://dx.doi.org/doi: 10.1016/j.jmst.2016.09.002
Reference: JMST 791

To appear in: *Journal of Materials Science & Technology*

Received date: 19-12-2015
Revised date: 15-3-2016
Accepted date: 8-4-2016

Please cite this article as: M. Mahbubur Rahman, Zhong-Tao Jiang, Chun-Yang Yin, Lee Siang Chuah, Hooi-Ling Lee, Amun Amri, Bee-Min Goh, Barry J. Wood, Chris Creagh, Nicholas Mondinos, Mohmmednoor Altarawneh, Bogdan Z. Dlugogorski, Structural Thermal Stability of Graphene Oxide-doped Copper-cobalt Oxide Coatings as a Solar Selective Surface, *Journal of Materials Science & Technology* (2016), http://dx.doi.org/doi: 10.1016/j.jmst.2016.09.002.

Structural Thermal Stability of Graphene Oxide-doped Copper-cobalt Oxide Coatings as a Solar Selective Surface

M. Mahbubur Rahman[1*], Zhong-Tao Jiang[1*], Chun-Yang Yin[2], Lee Siang Chuah[3], Hooi-Ling Lee[4], Amun Amri[5], Bee-Min Goh[6], Barry J. Wood[7], Chris Creagh[8], Nicholas Mondinos[1], Mohmmednoor Altarawneh[8], Bogdan Z. Dlugogorski[8]

[1]Surface Analysis and Materials Engineering Research Group, School of Engineering & Information Technology, Murdoch University, Murdoch, Western Australia 6150, Australia

[2]School of Science & Engineering, Teesside University, Borough Road, Middlesbrough, TS1 3BA, United Kingdom

[3]Department of Physics, School of Distance Education, Universiti Sains Malaysia, 11800 Minden, Penang, Malaysia

[4]Department of Chemistry, School of Chemical Sciences, Universiti Sains Malaysia, 11800 Minden, Penang, Malaysia

[5]Department of Chemical Engineering, Universitas Riau, Pekanbaru, Indonesia

[6]School of Chemistry, Bedson Building, Newcastle University, NE1 7RU, United Kingdom

[7]School of Chemistry, The University of Queensland, St. Lucia, QLD 4072, Australia

[8]School of Engineering & Information Technology, Murdoch University, Murdoch, Western Australia 6150, Australia

[Received 19 December 2015; received in revised form 15 March 2015; accepted 8 April 2016]

**Corresponding author. Tel. +61 8 9360 2867; E-mail address: Z.Jiang@murdoch.edu.au (Z-T. Jiang).

*Corresponding author: Tel. +61 8 9360 7372; E-mail address: M.Rahman@murdoch.edu.au (M.M. Rahman).

3d transition metal oxides based thin film coatings such as copper-cobalt oxides exhibit high absorption in the visible region and low emittance in the infra-red to far-infra-red region of the solar spectrum which is favourable for use as potential selective surface materials in photothermal devices. These materials have the potential to minimize heating while increasing absorption in the operative spectrum range and therefore achieve higher solar selectivity. A series of mixed copper-cobalt metal spinel oxides ($Cu_xCo_yO_z$) doped with graphene oxide thin films were deposited on commercial grade aluminium substrates using a sol–gel dip-coating technique at an annealing temperature of 500 °C in air for 1 h. Characterizations of the synthesized films were carried out by high temperature synchrotron radiation X-ray Diffraction (SR-XRD), UV-Vis, Fourier Transform infrared spectroscopy (FTIR) and X-ray photoelectron microscopy (XPS) techniques. High thermal stability of coatings with multiple phases, binary and ternary metal oxides, was defined through SR-XRD study. FTIR analysis shows moderate (<80%) to high (up to 99%) reflectance in the infra-red region while the UV-Vis investigations demonstrate that, in the visible region, solar absorption increases gradually (up to 95%) with the addition of graphene oxide to the $Cu_xCo_yO_z$ coatings. With the incorporation of 1.5 wt% of graphene oxide to the copper-cobalt oxide coatings, a high solar selectivity of 29.01 (the ratio of the average solar absorptance in visible and the average thermal emittance in infra-red to far infra-red region; α/ε) was achieved.

Key words: Coatings; Sol-gel method; Surface bonding; Thermal stability; Synchrotron radiation; Fourier transform infrared spectroscopy; X-ray diffraction; X-ray photoelectron spectroscopy

1. Introduction

Over the years, cobalt based mixed metal oxide thin films have been extensively studied by different groups around the world owing to their wide-spread applications[1–4]. Pure copper oxide[5], cobalt-copper oxide, manganese-cobalt oxide, nickel-cobalt oxide[6,7], and copper-aluminium oxide[8] have been used as high performance optical selector or absorbers. The physicochemical and electrochemical properties of $Cu_xCo_{3-x}O_4$ powder has been investigated for their practical applications as catalysts in oxygen evolutions reactions (EOR)[9]. There have been numerous investigations of mixed metal oxide thin films pursuing improved physicochemical, optical, thermal, electro-chemical, photo-chemical, magnetic, dielectric and electro-magnetic properties focusing on their potential practical applications in the areas such as clean energy devices, solar cells, photovoltaics, thermal collectors, solar selective absorbers, and smart windows. Optical characterizations, thermal durability studies, physicochemical and mechanical properties of sol-gel derived Cu–Co oxide coatings have been investigated by other groups[10,11]. In a recent study, Rahman et al.[12] reported the annealing temperature effects on the morphological, mechanical, solar selective characteristics and local electronic bonding states of metal nitride based thin film coatings. Synthesis mechanisms, cyclic stability and electrochemical performance of graphene-carbon nanotube hybrid films, graphene based

metal/metal oxides nanocomposite and nano-sized Co_3O_4 materials have been extensively discussed in earlier studies[13–15].

Optical applications of graphene oxide is also well-known[16]. The high optical absorption and tuneable optical band-gap are the most appealing characteristics of graphene that make it an ideal material for the effective light harnessing[17]. Light absorbing photovoltaic applications of graphene based materials have been reported in an earlier study[18]. Optical absorption and power conversion efficiency of layer-transferred graphene in organic hybrid solar cells have been reported[19]. The application of graphene in organic photovoltaic devices has been reported by Arco *et al.*[20] and Liu *et al.*[21]. Graphene has been reported to be a promising candidate for offering improved efficiency of light harvesting devices e.g., inorganic, organic[23,24], hybrid[25], and dye sensitized solar cells[26]. A series of comprehensive reviews focused on investigating manufacturing aspects, properties, and applications of graphene and graphene-based materials in energy related areas[27–29]. Optimization of optical properties of inorganic compounds mixing with graphene oxide forming a hybrid system is also feasible in the development of graphene oxide-based selective surface. As graphene oxide offers good solubility in aqueous and polar solvents, the sol-gel method is a feasible technique to prepare graphene oxide based thin films. These coatings exhibit high transmittance and the strong ability to resist abrasion, which make them suitable for applications in some harsh conditions.

In the past few years, numerous strategies have been adopted in the design of metal oxide based light harvesting assemblies. For instance, sol-gel derived mixed metal oxides based thin film selective solar surfaces attracted attention due to their flexibility and advantages e.g., cost-effective, good thermal and physicochemical stability, easy preparation process, shorter processing time, low-toxicity, less equipment needed, tuneable electronic band gap, and high

electron mobility. Despite the availability of numerous literature on metal oxide thin films and graphene oxide thin films for their optical and light harvesting purposes, however, to the best of our knowledge, utilization of mixed metal oxide with graphene oxide thin films as solar selective surface is yet to be explored. Nowadays, synchrotron radiation has emerged as a powerful and versatile analytical tool for materials production (*e.g.*, fabrication of microelectronic devices), quality control, and materials evaluation in industrial research and development. Synchrotron radiation possesses some salient features; very high intensity, high brightness, good stability, higher degree of polarization, wide energy range extending from infrared to X-ray wavelengths and so on. In synchrotron radiation, many different beamlines are involved and each beamline is designed for a specific type of research. For different beamlines, various techniques such as X-ray absorption, scattering, diffraction, and fluorescence analysis are available for synchrotron research. Synchrotron radiation facilities demonstrate superior capabilities to characterise various properties of materials. A wide range of experiments such as structure resolutions, variable temperature studies, structural studies of microporous materials, structure and property investigations of solid metal oxides, phase identification and quantification of pharmaceuticals ~~etc~~ can be successfully conducted at the synchrotron radiation-based powder diffraction (PD) beamline's primary end station. Synchrotron radiation-based spectroscopy is also used to investigate semiconductor and thin film surfaces to realize the interface formation among the constituents. Furthermore, the synchrotron radiation core level emission spectra, the chemical composition of the surface of the films, and the detection of the surface core level components can be used to explain the bonding configurations of the thin film coatings. The synchrotron radiation based spectroscopy thus assists revealing the interface formation and new development and applications can be evolved. For example, synchrotron radiation based near-edge X-ray

absorption fine structure (NEXAFS) initiated by the electron transfer from a core orbital to discrete or quasi-discrete unoccupied levels provide us with valuable information pertinent to the electronic structures and local atomic structures. The local bonding structures around a specific atom such as the coordination number, the bonding length, and the distribution of defects can be estimated by analysing the peak positions of synchrotron radiation based experiments. In a recent work[30], we conducted NEXAFS experiments to sol-gel derived copper-cobalt oxide coatings by measuring the Cu$L_{2,3}$-edges, Co$L_{2,3}$-edges and O *K*-edges. Our study demonstrated that the local environments of Cu, Co and O remained invariant with the change in the copper to cobalt concentration ratios except for the [Cu]/[Co] = 2 sample whereas the local coordination appeared to slightly change due to the loss of octahedral Cu^{+}. The Cu-L_3 and Cu-L_2 absorption edges arisen from the dipole transitions of the Cu2$p_{1/2}$ for L_2 and Cu2$p_{3/2}$ for L_3 into the empty *d* states while the Co-L_3 and Co-L_2 absorption edges appeared from Coulomb interactions and exchange interactions of 2*p* core holes with the 3*d* electrons. The hybridization of the Co3*d* states with O2*p* states and O2*p* states with Co4*sp* states and O2*p* states was extended to a Co higher orbital that was seen in the O *K*-edge NEXAFS peaks of copper-cobalt oxide coatings. In this study, we attempt to develop the graphene oxide as a mixture into the $Cu_xCo_yO_z$ systems for the development of the thin film based light harvesting devices with improved spectral selectivity. We focus on the structural thermal stability and optical effects of graphene oxide modified $Cu_xCo_yO_z$ composites in order to achieve better solar selective performance of coatings fabricated via dip-coating sol-gel technology.

2. Experimental Methods

2.1. *Sample preparation methodology*

Cobalt (II) chloride ($CoCl_2.6H_2O$, APS Chemical, >99%), copper (II) acetate monohydrate ($Cu(OOCCH_3)2.H_2O$, Alfa Aesar, >98%), propionic acid (C_2H_5COOH, Chem Supply, >99%), graphene oxide (concentration 1 mg/cc), and absolute ethanol (E. Mark of Germany, >99%.) were used to make the sols for synthesizing thin films. The highly-reflective commercial aluminium material (Anofol, size 2 cm × 4 cm) was used as substrate for the deposition of the coatings. The substrates were cleaned using a hot etching aqueous solution (85 °C) prepared by mixing chromium (VI) oxide and phosphoric acid for 10 min in order to remove the alumina layer. Substrates then were rinsed in hot mili-Q water followed by a flush of cooled mili-Q water and dried in a flow of high purity nitrogen gas.

In preparing the sols, cobalt (II) chloride ($CoCl_2 \cdot 6H_2O$, 0.25 mol/L), graphene oxide, and copper (II) acetate monohydrate ($Cu(OOCCH_3)_2 \cdot H_2O$ were mixed with absolute ethanol. Propionic acid (C_2H_5COOH) was used as the complexing agent to the solution. After stirring the mixed solution for 2 h, the resultant solution was used for thin film deposition on aluminium substrates using a dip-coating technique. The dip and withdrawal rate were 180 mm/min and 60 mm/min, respectively. The sample coating was heated at 150 °C for 60 s. A relative humidity of 50% was maintained during the entire period of the coatings preparation process. The same dip coating process, using same sol solution, was repeated four times to increase the thickness of film with better uniformity. Finally, the samples were annealed at 500 °C in air for 1 h. The heating rate of the furnace for annealing was kept at 50 °C/min and the samples were left in the furnace for 10 min after power was turned off.

2.2. *Characterizations of thin film coatings*

High resolution synchrotron radiation X-ray diffraction (SR-XRD) measurements of the $Cu_xCo_yO_z$ coatings with and without graphene oxide were conducted using the powder diffraction (PD) beamline 10-BM-1 at the Australian synchrotron, Melbourne. The PD beamline at Australian Synchrotron utilises a bending magnet source. The beamline was operated at 2.5 GeV which produces a continuous spectrum of photons in the range 5–30 keV with a maximum flux of about 10^{13} photons/s at an angular acceptance of 0.23 mrad vertical by 2.5 mrad horizontal. The samples were loaded in 0.3 mm diameter quartz capillaries with diamond powders that are rotated during the measurements. A MYTHEN II microstrip detector system was used in a 2θ = 18° to 44° geometry in steps of 0.002° for 5 min at each detector settings for SR-XRD data acquisition. The MYTHEN detector consists of 16 position sensitive detectors keeping a 0.2° gap between detector modules. X-rays of wavelength λ = 0.11267 nm as estimated with a LaB6 standard NIST 660a standard were used for SR-XRD measurements at a beam size of 7 mm in width and 1 mm in height with an exposure time of 145 min. High temperature measurements were achieved using an Anton Parr HTK20 furnace. The real time temperature was monitored by a thermocouple in direct contact with the bottom substrate of the coatings close to the irradiated area. The temperature difference between the top of the coating and the bottom of the substrate was calibrated before XRD measurement. The heating and cooling were remotely controlled via a computer interface. The acquired data were processed by using the PDViPeR software in order to obtain the XRD patterns as presented in Figs. 1 and 2.

Chemical analysis of the outermost 5–10 nm atomic layers of the thin film coatings was performed via the XPS technique. The Kratos Axis-Ultra photoelectron spectrometer uses Al *K*α monochromatic X-ray source with beam energy of 1486.6 eV at a power of ~10 mA and ~15 kV. Square size samples (2 mm × 2 mm) were mounted on steel sample holder. The pressure of the

XPS analyser chamber was maintained at 2.9×10^{-9} Torr. The Cu2*p*, Co2*p*, O1*s*, C1*s* photoelectron lines were recorded with a 2D delay line detector. The photoelectron energy scale was calibrated using C1*s* (hydrocarbon; C–H) line–at 284.6 eV. CASA-XPS (Version 2.3.15) software was employed for data processing and curve fitting in order to define the component of photoelectron lines.

The photon energy dependence of absorption coefficient helps to study the band structure and the type of electron transition involved in absorption process. In crystalline and amorphous materials the photon absorption obeys the Tauc relation[31–34],

$$\alpha h\nu = A(h\nu - E_g)^n \qquad (1)$$

where, α is the absorption coefficient, $h\nu$ is the incident photon energy, A is an energy independent constant, E_g is the band-gap energy and n is an index depending on the type of optical transition involved in photon absorption. The index n = 1/2 and 2 for direct and indirect allowed transitions and n = 3/2 and 3 for direct and indirect forbidden transitions, respectively[32]. Thus, the direct transition energy gap (direct band-gap energy) can be obtained by plotting $h\nu$ vs $(\alpha h\nu)^2$ and extrapolating the linear portion of the curve to $(\alpha h\nu)^2 = 0$ in the energy axis. Similarly the indirect energy band-gap can be found by plotting $h\nu$ vs $(\alpha h\nu)^{1/2}$ and extrapolating the linear portion of the curve to $(\alpha h\nu)^{1/2} = 0$ in the X-axis.

Solar absorptance of the coatings was determined using a double-beam UV–Vis spectrophotometer (Model: UV-670 UV-Vis spectrophotometer, JASCO, USA) with a unique, single monochromator design covering a wavelength range from 190 to 2200 nm. The monochromator consists of a 1200 grooves/mm grating and a photo multiplier tube (PMT)

detector for the UV-Vis measurements. The solar reflectance of the thin film coatings were measured using a FTIR spectrometer (Perkin Elmer Spectrum 100 FTIR Spectrometer, USA) in the wavelength of 2.5 to 15.5 µm. The solar absorptance and the thermal emittance of a material can be calculated from measurements of reflectance data from the-visible and infrared ranges of the solar spectrum[35]. For a range of solar wavelengths, the total solar absorptance, α is defined as a weighted fraction between absorbed radiation and incoming solar radiation (I_{sol}), while thermal emittance, ε is defined as a weighted fraction between emitted radiation and the Planck black-body distribution (I_p) and can be computed using Eqs. (2) and (3)[35]:

$$\alpha = \frac{\int_{0.19}^{2.2} I_{sol}(\lambda)(1 - R(\lambda))\,d\lambda}{\int_{0.19}^{2.5} I_{sol}(\lambda)\,d\lambda} \quad (2)$$

$$\varepsilon = \frac{\int_{2.5}^{15.4} I_p(\lambda)(1 - R(\lambda))\,d\lambda}{\int_{2.5}^{15.4} I_p(\lambda)\,d\lambda} \quad (3)$$

The solar spectrum, I_{sol} has an air mass (AM) of 1.5 in accordance with the ISO standard 9845-1 (1992). A key parameter of a selective surface is its selectivity, *s*, which is defined as a ratio of the solar absorptance (α) to the emittance (ε)[36] as given in Eq. (4):

$$s = \frac{\alpha}{\varepsilon} \quad (4)$$

where α signifies solar absorptance of the coatings estimated in a wavelength range of 190 nm and 2200 nm while ε is the emittance in a range between 2.5 µm and 15.5 µm.

3. Results and Discussion

3.1. Synchrotron radiation based high resolution XRD studies of the $Cu_xCo_yO_z$ thin film coatings

High temperature synchrotron radiation X-ray diffraction (SR-XRD) measurements of $Cu_xCo_yO_z$ with and without graphene oxide were carried out at room temperature, 100, 200 and 300 °C in a 2θ geometry from 18° to 44° and 0.002° increment. SR-XRD data presented in Fig. 1 provide information with the crystalline structures, phase transitions and thermal stability of these coatings. In CuCoO films, multiple and stable phases e.g., CuO_x, CoO_x, $CuCoO_x$ exist until to 300 °C. However $Cu_xCo_yO_z$ films with 1.5 wt% of graphene oxide, in addition to the above phases, a new phase orthorhombic/$CoCu_2O_3$ (space group $P_{mmn}(59)$) was also observed. Monoclinic CuO and hexagonal CoO were the dominant phases in each case (see details in Tables 1 and 2). All the coatings exhibited sharp diffraction lines at all temperatures indicating well defined crystalline phases. Absence of any impurity diffraction peaks reveals that the samples are formed with highly pure precursors. According to Table 1 and Table 2, it is clearly seen that the 2θ positions of all the existing phases are invariant at all measuring temperatures. This reflects the fact that these coatings possess good physical and chemical stability within the operating temperature up to 300 °C. Further observation shows that, with the addition of 1.5 wt% of graphene oxide to the copper-cobalt oxide coatings, 2θ positions of the Bragg reflections are slightly shifting towards the lower angle sides. Due to the lowering of 2θ values the residual stress of the coatings is reduced. The reduction in internal residual stresses result in lattice distortion. As a consequence of all these factors, it is believed that the coatings achieve greater mechanical and thermal stability in the operating temperature range. The existence of CuO and Co_3O_4 phases in Cu–Co spinel was detected by SR-XRD analysis. The phase crystallinity of deposited films is also in good agreement with the reported data for CoO[37]. However, the CuO lines show the relatively low intensity in the X-ray pattern on these coatings. Incorporation of the carbon materials into the mixed metal oxide networks leads to reduction of the scattering

intensities of the Bragg reflections. As a result, a subtle shift to smaller *d*-spacings takes place[38,39] and spinel structures with enhanced solar selectivity and better physical stability are attained. In these films, copper ions occupy both the tetrahedral and the octahedral sites of the spinels. The difference of ionic radius in the tetrahedral and octahedral sites of copper ions (16 pm) and cobalt ions (5.5 pm) also forms a basis for stable structural configurations of these coatings. The films are also stable towards air and moisture having well defined grain boundaries. Cu–Co oxide based thin films form a single phase together with a partially inverted spinel structure[40–44] and the segregation of Cu and/or Co oxide phases depends on the Cu/Co ratio and annealing temperatures. Compared to other methods the sol–gel dip-coating method allows the preparation of the Co_3O_4 stable phase at relatively low temperature[45]. Annealing of the coatings promotes the migration of the cobalt towards the surface of the coating, where it is oxidized by the atmospheric oxygen and forms the cobalt oxide layer. In a previous publication[46], annealing in air at 500 °C showed that the bulk cobalt films migrate towards the coating surface and forms a layer of Co_3O_4 having a thickness of 40–50 nm. Since the mixed CuCo oxide thin films can exist in a variety of compositions and crystal structures, their properties also vary widely. As a result, these coatings show a broad variety of potential applications[47] such as solar selective surfaces.

3.2. XPS analysis of the ($Cu_xCo_yO_z$ + graphene oxide) coatings

The XPS survey scans (not shown here) of these coatings were conducted before etching and after 2 min etching of each sample. An etching of 2 min was chosen to remove the surface contamination around the coatings. The elemental analyses of the copper cobalt oxide thin film coatings with the addition of various wt% of graphene oxide are presented in Table 3. From

Table 3, it is noticed that the carbon content is monotonically increased with the subsequent addition of graphene oxide to the copper cobalt oxide coatings which in turn indicates that the progressive amount of graphene oxide was introduced to the copper cobalt oxide coatings.

Fig. 2(a–e) exhibits the deconvolution of the XPS spectra of the Cu2$p_{3/2}$ peak of $Cu_xCo_yO_z$ coatings deposited with various wt.% of GO. The two main peaks of Cu2$p_{3/2}$ and Cu2$p_{1/2}$ (Cu2$p_{1/2}$ are not shown here) have a binding energy difference of 19.9 eV. The difference in binding energy between Cu2$p_{1/2}$ and Cu2$p_{3/2}$ peaks suggests the occurrence of low oxidation states of copper. Our findings herein are in accord with earlier reports[30,48]. Compared to the CuO, the covalent nature of the Cu–O bond in copper cobaltite was reduced due to the higher intensity of the satellite peak[49]. The deconvolution of Cu2$p_{3/2}$ photoelectron lines illustrates two curve-fitting components in the vicinity of 932–934.5 eV. The main Cu2$p_{3/2}$ peaks around 932-933 eV are due to the metal (octahedral) Cu^+ ions whereas peaks due to the Cu^{2+} ions were found at 934–935 eV. It is believed that the Cu2$p_{3/2}$ photoelectron peaks reveal the tetrahedral Cu^+ with its counterpart peak from the octahedral Cu^+[50]. The Cu2$p_{3/2}$ photoelectron peak with shake-up satellite is ascribed to the copper oxides. In copper cobalt oxide system, the reduction of Cu^{2+} to Cu^+ has been previously detected[49,51]. The oxidation state of copper with different coordinations is possibly due to the evolution of Cu^{2+} A-sites originating from the disintegration during the high-temperature annealing at 500 °C. Other reports mentioned that portion of octahedral Cu^{2+} (satellites of cupric oxide) further reduced to octahedral Cu^+[52,53]. The Cu^{2+} ions are merged into the surface octahedral vacancy, accommodating oxygen with neighboring Co^{2+} ions and thereby forming Cu–O–Co like species[49,54]. The Cu^+ and Cu^{2+} ions indicate the presence of Cu_2O and CuO in the copper-cobalt system. The presence of CuO was also confirmed by our synchrotron radiation XRD studies.

The XPS spectra of the Co2*p* peaks and the decomposition of the Co2$p_{3/2}$ peak of copper-cobalt oxide thin film coatings synthesized with various wt% of graphene oxide are presented in Fig. 3(a–e). In each of the Co2*p* spectrum, two main peaks are assigned as Co2$p_{3/2}$ and Co2$p_{3/2,}$ along with a satellite in the neighbourhood of the higher binding energy region of each peaks. In each coating, the peak-fitting of Co2$p_{3/2}$ and its satellite give rises to three components (See Fig. 3(a–e)). Peaks Co2$p_{3/2}$ and Co2$p_{3/2}$ are separated (not shown here) with binding energy of ~16 eV due to the spin-orbit coupling of mixed Co^{2+} and Co^{3+} ions. The existence of the satellite in the neighbourhood of Co2$p_{3/2}$ peak implies that the feature of Co ions is occupied in a partial spinel crystal structure. The low intensity of the satellites also confirms the presence of Co^{3+} ions mixing with Co^{2+} ions[41]. The components i and ii are due to the formation of Co_3O_4, and Co_2O_3 which are mostly due to octahedral Co^{3+} or mixed Co^{2+} and Co^{3+} bonding states.

Formation of Co_3O_4 was also revealed in the high resolution X-ray diffraction studies employed by synchrotron radiation. Since the binding energy of Co^{2+} is higher than that of Co^{3+}, the shake-up satellite was mostly recorded above 785 eV and is identified to be contributedfrom cobalt oxide bonds. From the Cu2$p_{3/2}$ features, characteristic of copper (Cu^{+2}) oxides in tetrahedral coordination, it is seen that the Cu^{2+} ions partially substitute the Co^{2+} ions thus forming a lower degree of crystallization of $Cu^{2+}Co_2{}^{3+}O_4$ spinel systems[9,30].

Fig. 4(a–e) demonstrates the O1*s* XPS spectra and the corresponding curve-fitting arisen from the decomposition O1*s* peak of $Cu_xCo_yO_z$ coatings without and with various wt.% of graphene oxide. The decomposition of O1*s* peak and the satellite give out three curve fitting components (Fig. 4(a–e)). All the O1*s* spectrum shows a strong peak with a shoulder at the high energy side which is a typical feature of $Cu_xCo_yO_z$ coatings[9]. Comparatively, flat shoulder peak in the high energy side of O1*s* peak arises from the high volume fraction of surface oxygen and

the low amount of subsurface oxygen in the coated films. Further, the shoulders at the high energy side of the O1*s* peaks are the characteristic feature of the copper-cobalt oxide systems that differentiates them from O1*s* on Co_3O_4[9]. The decoupling curve-fitting peaks (on the lower energy side) are mostly due to the lattice O^{2-} in a Co_3O_4 spinel structure while the other peaks (on the higher energy side) are due to the OH-originated groups *e.g*., carbonate, hydroxyl etc[9,41,49,55,56]. It is also assumed that these peaks are arisen from (Cu–O, Co–O) covalent bonds[30,41].

The deconvolution of high resolution C1*s* XPS data and their corresponding peak-fitting of copper fitting components above 286 eV and 288 eV are the surface contamination of the oxygen, surface oxygen such as chemisorbed water or chemisorbed oxygen O^- etc introduced during the synthesis and annealing processes of the thin film coatings. In a bulk structure, the oxygen ions near the surface, generally, have lower electron density than the lattice O^{2-} ions[57]. It is also seen that the coordination number of oxygen ions is much smaller than in cobalt oxide thin film coatings with and without the addition of various wt.% of graphene oxide (Fig. 5). The C1*s* XPS spectra display a single peak at 284.6 eV together with an asymmetrical tail at high energy side. The principal component of decoupled peak represents the graphitic carbon or hydrocarbon bonds (C–C/C–H bonds) at 284.60 eV and the remainder a regular site together with stronger metal-oxygen assigned as C–OH/C–O–C and C=O/O=C–O structures originated from graphite stacking material[58]. In Ref. [59], π–π* shake-up at higher energy side corresponding to sp^2 hybridized carbon was noticed. However, in the present investigation no π–π* shake-up was identified. A reduction in the peak intensities of C=O/O=C–O bonds was seen on the deconvoluted C1*s* peak and indicates the incomplete removal of the carbonyl, hydroxyl, and epoxy groups (originated from the oxidation and destruction of the sp^2 bonded pristine

graphene) after the heat treatment[60]. The C=O bonds were detected at 288.01–288.40 eV which eventually confirmed the presence of C=O bonds observed in O1*s* spectra at 531.33–531.44 eV. Detailed XPS results of $Cu_xCo_yO_z$ and $Cu_xCo_yO_z$/graphene oxide coatings are tabulated in Table 4. The XPS fitting curves of Cu2$p_{3/2}$, Co2$p_{3/2}$, O1*s* and C1*s* spectra were analysed via CASA XPS 2.3.1.5 software. A slight change in peaks broadening and peaks shifting towards the lower binding energy was noticed while controlled amount of graphene oxide were incorporated to the sol-gel derived copper-cobalt oxide coatings. This peak shifting and peak broadening indicates the appearance of the reduced states of Cu and Co species on the surface. This also reveals the occurrence of a larger number of oxygen vacancies around the surface of the films. However, a subtle peak shift observed in C1*s* peak towards the higher binding energies reveals that the presence of graphene oxide modifies the bonding environments of the carbon atoms. It is probably due to the variation in the relative proportions of carbon-carbon and carbon-oxygen contributions. The XPS-peak intensity of all the five samples is identical although measured peak intensities varied significantly with the addition of graphene oxide to the copper-cobalt oxide films. However, to realize the substantial information of measured XPS peak intensities depth profile analysis of the atoms is essential.

3.3. Energy band-gaps of ($Cu_xCo_yO_z$ + graphene oxide) coatings

The UV-Vis absorptance spectra presented in Fig. 6 were used to inspect the optically induced transition and to acquire information about the band structure of the films. Fig. 6 shows that in the visible range of the spectra, the solar absorptance of these coatings increases with the increase in wavelengths. At a wavelength of 350–460 nm, the absorbance values reach its maximum and then decreases. Another maxima was detected at a wavelength of 1360–1500 nm.

The spectral dependence of α on the photon energy ($h\nu$) helps to estimate the energy band-gaps of a material. Photon absorptions in crystalline and amorphous materials are known to follow the Tauc relation as given in Eq. (1). The energy band-gap, E_g involved in CuCoO coatings with and without the addition of graphene oxide was estimated by Tauc plot, by plotting the function $(\alpha h\nu)^2$ vs $h\nu$ (the photon energy), by extrapolating the linear portion of the curve to zero absorption. Tauc plots of $h\nu$ vs $(\alpha h\nu)^2$ for CuCoO coatings with and without the addition of graphene oxide films are shown in Fig. 7 and energy gaps were estimated from the intercepts of the linear part of the curves extrapolated to zero in the photon energy axis. The energy band-gap values computed for CuCoO coatings with and without the addition of graphene oxide films are presented in Table 5. The values of direct and indirect transition energy gaps lie between 1.6 and 2.4 eV. From Table 5 it is found that the energy band-gaps of CuCoO coatings slightly decrease with the subsequent incorporation of graphene oxide to the CuCoO system. This decrease in energy band-gaps play significant role in enhancing the photon absorption capability of these coatings with the subsequent addition of graphene oxide to the CuCoO matrix.

3.4. Optical properties of mixed ($Cu_xCo_yO_z$ + graphene oxide) coatings

Fig. 8 shows the UV-Vis spectra of $Cu_xCo_yO_z$ thin film coatings on aluminum substrates with and without the progressive addition of graphene oxide. The solar absorptance of the coatingswas calculated based on the AM1.5 solar spectrum standard using the hemispherical reflectance data. This was recorded via UV–Vis-NIR Jasco V-670 double beam spectrophotometer with 60 mm integrating sphere in the wavelength range of 190 to 2200 nm. The solar absorptance values estimated in terms of reflectance as described by Duffie and Beckman[35] are displayed in Table 6. The UV-Vis reflectance data presented in Fig. 8, indicate that the coatings offer low reflectance (<50%) to UV light, moderate reflectance (<80%) in the

visible spectrum and high reflectance (up to 100%) in the region from infrared to far-infrared of the solar spectrum. In the shorter wavelength region, all the UV-Vis spectra are similar showing an interference peaks and absorption edges which is consistent with previous study by Amir *et al.* [7]. The solar absorptance of the coatings without graphene oxide was found to be 83.4%, however with the addition of 1.5 wt% of graphene oxide, the absorptance increased to 86.14%. Thus, the introduction of controlled amount of graphene oxide to the $Cu_xCo_yO_z$ thin film coatings, the solar absorptance increased significantly. This superior absorptance would make them smart candidates for their practical application as a selective surface. This result is in good agreement with earlier reported sol-gel derived coatings[61–63]. Optical absorptance of the copper–cobalt oxide films is influenced by the film thickness, the composition of the substrate, the roughness of the film surface and surface pores among others. Aluminium substrate was used for the films because of its low cost and high reflectivity[6]. The highly reflective aluminium surface serves to reflect back the infra-red radiation that penetrates the film coating. The copper-cobalt films deposited on the aluminium substrate significantly exhibit higher degree of solar absorption compared to that deposited on a glass substrate[6]. A rough surface results in a decrease in reflection of the incident solar energy from the surface and the refractive index is reduced by the presence of pores in the $Cu_xCo_yO_z$ graphene oxide surface. These factors promote the solar absorptance by means of multiple reflections and resonant scattering in the pores.

Fig. 9 shows the FTIR spectra of $Cu_xCo_yO_z$ thin film coatings with and without the addition of graphene oxide in the wavelength range of 2.5 to 15.5 µm. The thermal emittance of the coatings was calculated in terms of reflectance as described by Duffie and Beckman[35] and the corresponding solar selectivity was computed. Results of such calculations are displayed in Table 6. From our measurements, it is observed that in the infra-red and far infra-red region, the

solar emittance of the coatings decreased significantly with the progressive addition of the graphene oxide to the $Cu_xCo_yO_z$ thin film coatings. This reveals that graphene oxide plays a remarkable role in improving the selectivity of the $Cu_xCo_yO_z$ coatings which reduces the energy loss of the selective surface substantially in the infrared region of the spectrum. In all coatings, interference peak and absorption edge were detected at the shorter wavelength sides. It is well known that the interference peaks and the absorption edges are shifted towards the longer wavelengths regions subsequently when graphene oxide was added to the copper-cobalt films. With the incorporation of 1.5 wt% of graphene oxide in the copper-cobalt oxide films, a highest absorptance of 95.19% was achieved while the average absorptance calculated via D-B method[35] was 86.14%. Relatively weaker phonon absorption in the vicinity of the wavelength range of 15 μm is also typically exhibited by the copper-cobalt oxide system. Following the same method as described in Ref. [35], an average thermal emittance of 2.97% was recorded by the copper-cobalt coatings doped with 1.5 wt% of graphene oxide and thereby a high solar selectivity of 29.01 was attained for this coating. The increase of absorptance after the addition of graphene oxide is referred to the reduction of reflective properties of coating surface. This variation of reflective properties is attributed to the interference phenomena governed by film thickness and refractive index ratios. A non-uniform and inhomogeneous surface reduces the reflection of the incoming solar radiation at the film surface together with the lower refractive index. At the same time, multiple reflections and resonant scattering of the incident solar radiation also take place around the film surface[64]. As a result, the solar absorptance is raised up due to the interaction and relaxation mechanisms in the coatings. The higher value of solar absorptance appears to be very promising for application of solar selective surface in photothermal collectors. Compared with other reports for sol-gel derived coatings whereby their

α = 83%[63], 80%–85%[61] and 80%[62], our findings are quite encouraging. We further assume that the highly reflective aluminium substrates benefits to reflect back the infrared light that pass through the coatings without being absorbed. The transmitted light is reflected back by the substrate which increases the reflectance and reduces the absorptance in the near infrared (NIR) range. As a result, a dark mirror absorber-reflector tandem concept is virtually produced. The solar absorptance and emittance data manifest the fact that addition of a controlled amount of graphene oxide to the copper cobalt oxide coating increases solar selectivity due to the high absorptance in the visible region and increased reflectance in the region from infrared to far-infrared of the solar spectrum. Thus, copper–cobalt oxide thin film coatings with the addition of graphene oxide have a great potential to form the basis of an absorber material for solar selective surface applications in photothermal devices.

4. Conclusion

The structural characterization, solar selectivity and X-ray photoelectron spectroscopic investigations of the sol-gel derived copper-cobalt oxide thin film coatings with addition of graphene oxide has been investigated. Synchrotron radiation-based high resolution XRD tests show existence of physically, thermally and chemically stable multiple phases. The energy band-gaps of these coatings were found to decrease systematically with the progressive addition of graphene oxide to the CuCoO films. The solar absorptance was found to increase with the progressive addition of graphene oxide to the $Cu_xCo_yO_z$ system while the optical emittance was reduced and thereby the solar selectivity was significant increased. Hence, copper cobalt oxide thin films with the addition of graphene oxide display a good promise as a smart solar selective surface for photothermal applications. Such features are interesting aspects which may be

prevalent in future research concerning designs of superior selective surface. In the present study, we have adopted the sol-gel dip coating method to fabricate mixed metal oxides-based thin film coatings. Sol-gel dip-coating is a popular and versatile technique that can produce mixed metal oxides based thin film coatings with very high solar selectivity up to 44.23. Surface analysis of these coatings via XPS route confirmed the presence of various metal oxide phases (*e.g.*, Cu_2O, CuO, Co_3O_4) which protect them from further oxidization and corrosion. As a solar selective surface, these types of coatings possess some unique advantages e.g., easy operation, convenient and environment friendly, higher efficiency coupled with lower processing costs over other conventional techniques.

Acknowledgements

M.M. Rahman would like to thank Murdoch International Postgraduate Research Scholarship (MIPRS) program to carry out his PhD research.The authors also acknowledge Australian synchrotron for providing Powder Diffraction beamtime (AS141/PD/7582). C.Y. Yin is supported by the Teesside University Research Fund (URF). The authors also acknowledge funding support provided by IRU-MRUN Collaborative Research Program-2015.

References

[1] A.V. Chadwick, S.L.P. Savin, S. Fiddy, R. Alcántara, D.F. Lisbona, P. Lavela, G.F. Ortiz, J.L. Tirado, J. Phys. Chem. C 111 (2007) 4636–4642.

[2] R. Alcántara, M. Jaraba, P. Lavela, J.L. Tirado, Chem. Mater. 14 (2002) 2847–2848.

[3] A. Balland, P. Gannon, M. Deibert, S. Chevalier, G. Caboche, S. Fontana, Surf. Coat. Technol. 203 (2009) 3291–3296.

[4] T.Y. Wei, C.H. Chen, H.C. Chien, S.Y. Lu, C.C. Hu, Adv. Mater. 22 (2010) 347–351.

[5] X. Xiao, L. Miao, G. Xu, L. Lu, Z. Su, N. Wang, S. Tanemura, Appl. Surf. Sci. 257 (2011) 10729–10736.

[6] A. Amri, Z.T. Jiang, T. Pryor, C.Y. Yin, Z. Xie, N. Mondinos, Surf. Coat. Technol. 207 (2012) 367–374.

[7] A. Amri, X. Duan, C.Y. Yin, Z.T. Jiang, M.M. Rahman, T. Pryor, Appl. Surf. Sci. 275 (2013) 127–135.

[8] D. Ding, W. Cai, M. Long, H. Wu, Y. Wu, Sol. Energy Mater. Solar Cells 94 (2010) 1578–1581.

[9] M. De Koninck, S.C. Poirier, B. Marsan, J. Electrochem. Soc. 153 (2006) A2103-A2110 .

[10] A. Amri, Z.T. Jiang, N. Wyatt, C.Y. Yin, N. Mondinos, T. Pryor, M.M. Rahman, Ceramics Int. 40 (2014) 16569–16575.

[11] A. Amri, Z.T. Jiang, X. Zhao, Z. Xie, C.Y. Yin, N. Ali, N. Mondinos, M.M. Rahman, D. Habibi, Surf. Coat. Technol. 239 (2014) 212–221.

[12] M.M. Rahman, Z.T. Jiang, Z.F. Zhou, Z. Xie, C.Y. Yin, H. Kabir, M.M. Haque, A. Amri, N. Mondinos, M. Altarawneh, J. Alloy. Compd. 671 (2016) 254–266.

[13] A.W. Anwar, A. Majeed, N. Iqbal, W. Ullah, A. Shuaib, U. Ilyas, F. Bibi, H.M. Rafique, J. Mater. Sci. Technol. 31 (2015) 699–707.

[14] C. Hu, J. Guo, J. Wen, Y. Peng, J. Mater. Sci. Technol. 29 (2013) 215–220.

[15] N. Van Chuc, C.T. Thanh, N. Van Tu, V.T.Q. Phuong, P.V. Thang, N.T. Thanh Tam, J. Mater. Sci. Technol. 31 (2015) 479–483.

[16] K.P. Loh, Q. Bao, G. Eda, M. Chhowalla, Nat. Chem. 2 (2010) 1015–1024.

[17] X. Huang, Z. Yin, S. Wu, X. Qi, Q. He, Q. Zhang, Q. Yan, F. Boey, H. Zhang, Small 7 (2011) 1876–1902.

[18] M.T. Ong, E.J. Reed, ACS Nano 6 (2012) 1387–1394.

[19] Z. Wang, C.P. Puls, N.E. Staley, Y. Zhang, A. Todd, J. Xu, C.A. Howsare, M.J. Hollander, J.A. Robinson, Y. Liu, Physica E 44 (2011) 521–524.

[20] L. Gomez De Arco, Y. Zhang, C.W. Schlenker, K. Ryu, M.E. Thompson, C. Zhou, ACS Nano 4 (2010) 2865–2873.

[21] Q. Liu, Z. Liu, X. Zhang, L. Yang, N. Zhang, G. Pan, S. Yin, Y. Chen, J. Wei, Adv. Func. Mater. 19 (2009) 894–904.

[22] F. Yavari, C. Kritzinger, C. Gaire, L. Song, H. Gulapalli, T. Borca-Tasciuc, P.M. Ajayan, N. Koratkar, Small 6 (2010) 2535–2538.

[23] G. Jo, S.I. Na, S.H. Oh, S. Lee, T.S. Kim, G. Wang, M. Choe, W. Park, J. Yoon, D.Y. Kim, Y.H. Kahng, T. Lee, F. Yavari, C. Kritzinger, C. Gaire, L. Song, H. Gulapalli, T. Borca-Tasciuc, P.M. Ajayan, N. Koratkar, Appl. Phys. Lett. 97 (2010) 2535–2538.

[24] Y. Wang, X. Chen, Y. Zhong, F. Zhu, K.P. Loh, M. Choe, B.H. Lee, G. Jo, J. Park, W. Park, S. Lee, W.K. Hong, M.J. Seong, Y.H. Kahng, K. Lee, T. Lee, Appl. Phys. Lett. 95 (2009) 1864–1869.

[25] M. Choe, B.H. Lee, G. Jo, J. Park, W. Park, S. Lee, W.K. Hong, M.J. Seong, Y.H. Kahng, K. Lee, T. Lee, Organic Electronics: Phys. Mater. Appl. 11 (2010) 1864–1869.

[26] X. Wang, L. Zhi, K. Müllen, Nano Lett. 8 (2008) 323–327.

[27] B. Luo, S. Liu, L. Zhi, Small 8 (2012) 630–646.

[28] X. Huang, X. Qi, F. Boey, H. Zhang, Chem. Soc. Rev. 41 (2012) 666–686.

[29] W. Choi, I. Lahiri, R. Seelaboyina, Y.S. Kang, Crit. Rev. Solid State Mater. Sci. 35 (2010) 52–71.

[30] A. Amri, Z.T. Jiang, P.A. Bahri, C.Y. Yin, X. Zhao, Z. Xie, X. Duan, H. Widjaja, M.M. Rahman, T. Pryor, J. Phys. Chem. C 117 (2013) 16457–16467.

[31] K. Subramanyam, N. Sreelekha, D. Amaranatha Reddy, G. Murali, B. Poornaprakash, S. Ramu, R.P. Vijayalakshmi, Solid State Sci. 39 (2015) 74–81.

[32] B.D. Viezbicke, S. Patel, B.E. Davis, D.P. Birnie, III, Phys. Status Solidi B Basic Res. 252 (2015) 1700–1710.

[33] Z.T. Jiang, K. Ohshimo, M. Aoyama, T. Yamaguchi, Jpn. J. Appl. Phys. 37 (1998) 4008–4013.

[34] H. Kabir, M.M. Rahman, T.S. Roy, A. Bhuiyan, Int. J. Mech. Mechatronics Eng. 12 (2012) 30–34.

[35] A. Millar, M.M. Rahman, Z.-T. Jiang, J. Adv. Phys. 3 (2014) 179–193.

[36] T. Maruyama, Solar Energy Mater. Solar Cells 56 (1998) 85–92.

[37] I.K. Suh, H. Ohta, Y. Waseda, J. Mater. Sci. 23 (1988) 757–760.

[38] M. Fröba, R. Köhn, G. Bouffaud, O. Richard, G. Van Tendeloo, Chem. Mater. 11 (1999) 2858–2865.

[39] R. Köhn, M. Fröba, Catalysis Today 68 (2001) 227–236.

[40] S. Angelov, E. Zhecheva, K. Petrov, D. Menandjiev, Mater. Res. Bull. 17 (1982) 235–240.

[41] J.L. Gautier, E. Trollund, E. Ríos, P. Nkeng, G. Poillerat, J. Electroanal. Chem. 428 (1997) 47–56.

[42] G.H. Li, L.Z. Dai, D.S. Lu, S.Y. Peng, J. Solid State Chem. 89 (1990) 167–173.

[43] P. Stefanov, I. Avramova, D. Stoichev, N. Radic, B. Grbic, T. Marinova, Appl. Surf. Sci. 245 (2005) 65–72.

[44] T.C. Wen, H.M. Kang, Electrochim. Acta 43 (1998) 1729–1745.

[45] M. El Baydi, G. Poillerat, J.L. Rehspringer, J.L. Gautier, J.F. Koenig, P. Chartier, J. Solid State Chem. 109 (1994) 281–288.

[46] A. Ramos-Mendoza, H. Tototzintle-Huitle, A. Mendoza-Galván, J. González-Hernández, B.S. Chao, J. Vac. Sci. Technol. A 19 (2001) 1600–1605.

[47] V.G. Kessler, Chem. Commun. 9 (2003) 1213–1222.

[48] J. Xu, P. Gao, T.S. Zhao, Ener. Environ. Sci. 5 (2012) 5333–5339.

[49] A. La Rosa-Toro, R. Berenguer, C. Quijada, F. Montilla, E. Morallón, J.L. Vázquez, The J. Phys. Chem. B 110 (2006) 24021–24029.

[50] W.C. Oliver, G.M. Pharr, J. Mater. Res. 19 (2004) 3–20.

[51] A.C. Tavares, M.I. Da Silva Pereira, M.H. Mendonça, M.R. Nunes, F.M. Costa, C.M. Sá, J. Electroanal. Chem. 449 (1998) 91–100.

[52] Y. Li, J. Zhao, J. Han, X. He, Mater. Res. Bull. 40 (2005) 981–989.

[54] Y. Lv, L. Liu, H. Zhang, X. Yao, F. Gao, K. Yao, L. Dong, Y. Chen, J. Colloid Interf. Sci. 390 (2013) 158–169.

[54] Y. Lv, H. Zhang, Y. Cao, L. Dong, L. Zhang, K. Yao, F. Gao, L. Dong, Y. Chen, J. Colloid Interf. Sci. 372 (2012) 63–72.

[55] Y.Y. Peng, T.E. Hsieh, C.H. Hsu, Nanotechnology 17 (2006) 174–180.

[56] G. Tyuliev, D. Panayotov, I. Avramova, D. Stoichev, T. Marinova, Mater. Sci. Eng. C 23 (2003) 117–121.

[57] S. Royer, A. Van Neste, R. Davidson, B. McIntyre, S. Kaliaguine, Indus. Eng. Chem. Res. 43 (2004) 5670–5680.

[58] A. Safavi, M. Tohidi, F.A. Mahyari, H. Shahbaazi, J. Mater. Chem. 22 (2012) 3825–3831.

[59] H.L. Poh, F. Sanek, A. Ambrosi, G. Zhao, Z. Sofer, M. Pumera, Nanoscale 4 (2012) 3515–3522.

[60] S. Pei, J. Zhao, J. Du, W. Ren, H.M. Cheng, Carbon 48 (2010) 4466–4474.

[61] L. Kaluža, B. Orel, G. Dražič, M. Kohl, Solar Energy Mater. Solar Cells 70 (2001) 187–201.

[62] E. Barrera, L. Huerta, S. Muhl, A. Avila, Solar Energy Mater. Solar Cells 88 (2005) 179–186.

[63] T. Boström, E. Wäckelgård, G. Westin, Solar Energy 74 (2003) 497–503.

[64] M.E. Rincón, J.D. Molina, M. Sánchez, C. Arancibia, E. García, Solar Energy Mater. Solar Cells 91 (2007) 1421–1425.

Table 1. 2θ positions, crystal phases, Miller indices and space groups of sol-gel derived $Cu_xCo_yO_z$ coatings as observed from synchrotron radiation XRD studies.

2θ position at room temperature	2θ position at 100°C	2θ position at 200°C	2θ position at 300°C	Crystal structure	Miller index	Space group	JCPDS reference
20.11 (A)	20.09	20.08	20.08	Monoclinic/CuO	(200)	Cc(9)	89-5899
20.48 (B)	20.44	20.46	20.47		(111)		
36.76 (F)	33.75	33.77	33.76		(022)		
41.59 (J)	41.56	41.56	41.58		(222)		
20.11 (A)	20.11	20.10	20.09	Cubic/$CoCo_2O_4$	(222)	Fd-3m(227)	78-1980
23.28 (C)	23.28	23.26	23.26		(400)		
33.76 (F)	33.75	33.77	33.76		(440)		
39.15 (G)	39.16	39.14	39.13		(622)		
20.11 (A)	20.10	20.09	20.10	Hexagonal/CoO	(101)	$P6_3mc$(186)	89-2803
33.16 (E)	33.13	33.15	33.14		(103)		
39.91 (H)	39.90	39.89	39.89		(202)		
40.98 (I)	40.96	40.97	40.97		(104)		
23.84 (D)	23.84	23.85	23.83	Rhombohedral/$CoCuO_2$	(221)	R-3m(166)	74-1855
33.76 (F)	33.75	33.75	33.75		(444)		
39.91 (H)	39.90	39.88	39.89		(020)		
41.59 (J)	41.58	41.57	41.59		(131)		
39.15 (G)	39.14	39.13	39.13		(316)		

607

608 **Table 2.** 2θ Positions, crystal phases, Miller indices and space groups of sol-gel derived

609 ($Cu_xCo_yO_z$ + 1.5 wt% GO) coatings as observed from synchrotron radiation XRD studies.

2θ position at room temperature	2θ position at 100°C	2θ position at 200°C	2θ position at 300°C	Crystal structure	Miller index	Space group	JCPDS reference
20.10 (A)	20.09	20.08	20.08	Monoclinic/CuO	(200)	Cc(9)	89-5899
20.48 (B)	20.45	20.46	20.47		(111)		
33.74 (F)	33.73	33.74	33.74		(022)		
41.57 (J)	41.56	41.56	41.57		(222)		
20.11 (A)	20.11	20.10	20.09	Cubic/$CoCo_2O_3$	(222)	Fd-3m(227)	78-1980
23.28 (C)	23.28	23.26	23.26		(400)		
33.76 (F)	33.75	33.77	33.76		(440)		
39.15 (G)	39.16	39.14	39.13		(622)		
20.11 (A)	20.10	20.09	20.10	Hexagonal/CoO	(101)	$P6_3mc$(186)	89-2803
33.16 (E)	33.13	33.15	33.14		(103)		
39.91 (H)	39.90	39.89	39.89		(202)		
40.98 (I)	40.96	40.97	40.97		(104)		
23.84 (D)	23.82	23.83	23.83	Rhombohedral/ $CoCuO_2$	(221)	R-3m(166)	74-1855
33.74 (F)	33.73	33.73	33.74		(444)		
39.90 (H)	39.90	39.89	39.89		(020)		
41.57 (J)	41.57	41.57	41.56		(131)		
20.48 (B)	20.84	20.47	20.47	Orthorhombic/Co Cu_2O_3	(301)	Pmmn(59)	76-0442
23.84 (D)	23.83	23.84	23.83		(020)		
33.74 (F)	33.74	33.73	33.74		(302)		
39.10 (G)	39.10	39.10	39.09		(620)		

610

611

612

613

614

615

616

617

Table 3. Atomic compositions of $Cu_xCo_yO_z$ thin film coatings with and without graphene oxide addition before and after etching as estimated via XPS measurements.

Samples	Elements	Atomic percentages (at.%) of elements	
		Before etching	After etching
$Cu_xCo_yO_z$	Cu	12.54	28.66
	Co	11.67	33.51
	O	43.11	33.82
	C	32.67	4.01
$Cu_xCo_yO_z$ +0.1wt%GO	Cu	14.46	30.57
	Co	20.58	35.45
	O	40.92	28.66
	C	24.04	5.32
$Cu_xCo_yO_z$ +0.5wt%GO	Cu	19.13	29.87
	Co	20.27	34.66
	O	36.08	30.09
	C	24.52	5.38
$Cu_xCo_yO_z$ +1.0wt%GO	Cu	12.96	30.35
	Co	15.75	36.71
	O	40.55	27.41
	C	30.74	5.54
$Cu_xCo_yO_z$ +1.5wt%GO	Cu	14.41	28.47
	Co	17.83	30.02
	O	39.03	35.19
	C	28.73	6.32

630

631 **Table 4.** Fitting results of the XPS data of sol-gel derived $Cu_xCo_yO_z$ coatings with and without

632 graphene oxide addition for the core level binding energies.

Samples	Photoelectron lines	Bonding states	BE (eV)	FWHM (eV)	Percentage of the component (%)
$Cu_xCo_yO_z$	Cu2*p3/2*	Metal Cu^+ ions (Cu_2O bonds)	932.52(i)	1.70	68.86
		Metal Cu^{2+} ions (CuO bonds)	934.55(ii)	2.00	31.14
	Co2*p3/2*	Co_3O_4	779.40(i)	2.00	24.54
		Co_2O_3	781.15(ii)	3.26	37.34
	Co2*p3/2* sat.	Co_3O_4/Co_2O_3	785.96(iii)	5.96	38.12
	O1*s*	Metal oxides (Cu/Co oxides)	529.26(i)	1.00	54.33
		Metal oxides (Cu/Co oxides)	529.81(ii)	1.30	28.07
		Surface oxygen/C=O/O=C-O bonds	531.37(iii)	1.30	17.60
	C1*s*	C-C/C-H bonds	284.40(i)	1.30	60.25
		C-OH/C-O-C bonds	286.28(ii)	1.25	23.01
		C=O/O=C-O bonds	288.14(iii)	1.30	16.74
$Cu_xCo_yO_z$ + 0.1wt%GO	Cu2*p3/2*	Metal Cu^+ ions (Cu_2O bonds)	932.53(i)	1.80	74.03
		Metal Cu^{2+} ions (CuO bonds)	934.45(ii)	2.20	25.97
	Co2*p3/2*	Co_3O_4	779.15(i)	2.00	30.75
		Co_2O_3	780.94(ii)	3.30	35.29
	Co2*p3/2* sat.	Co_3O_4/Co_2O_3	785.78(iii)	6.00	33.96
	O1*s*	Metal oxides (Cu/Co oxides)	529.24(i)	1.07	60.10
		Metal oxides (Cu/Co oxides)	529.78(ii)	1.35	18.58
		Surface oxygen/C=O/O=C-O bonds	531.13(iii)	1.50	21.31
	C1*s*	C-C/C-H bonds	284.45(i)	1.32	72.82
		C-OH/C-O-C bonds	286.62(ii)	1.32	14.59
		C=O/O=C-O bonds	288.01(iii)	1.32	12.59
$Cu_xCo_yO_z$ + 0.5wt%GO	Cu2*p3/2*	Metal Cu^+ ions (Cu_2O bonds)	932.40((i)	1.70	73.97
		Metal Cu^{2+} ions (CuO bonds)	934.30(ii)	1.74	26.03
	Co2*p3/2*	Co_3O_4	779.12(i)	2.00	28.66
		Co_2O_3	780.86(ii)	3.30	34.08
	Co2*p3/2* sat.	Co_3O_4/Co_2O_3	785.71(iii)	5.97	37.25
	O1*s*	Metal oxides (Cu/Co oxides)	529.15(i)	1.08	63.38
		Metal oxides (Cu/Co oxides)	529.71(ii)	1.32	13.97
		Surface oxygen/C=O/O=C-O bonds	531.10(iii)	1.68	22.65
	C1*s*	C-C/C-H bonds	284.34(i)	1.34	78.09
		C-OH/C-O-C bonds	286.79(ii)	1.32	11.24
		C=O/O=C-O bonds	288.58(iii)	1.33	10.68
$Cu_xCo_yO_z$ + 1wt%GO	Cu2*p3/2*	Metal Cu^+ ions (Cu_2O bonds)	932.34(i)	1.77	67.96
		Metal Cu^{2+} ions (CuO bonds)	934.28(ii)	2.20	32.04
	Co2*p3/2*	Co_3O_4	779.08(i)	2.00	25.47
		Co_2O_3	780.80(ii)	3.29	37.26
	Co2*p3/2* sat.	Co_3O_4/Co_2O_3	785.67(iii)	5.99	37.27
	O1*s*	Metal oxides (Cu/Co oxides)	529.06(i)	1.10	61.14
		Metal oxides (Cu/Co oxides)	529.49(ii)	1.35	28.93
		Surface oxygen/C=O/O=C-O bonds	530.98(iii)	1.39	9.93

	C1*s*	C-C/C-H bonds	284.37(i)	1.40	62.84
		C-OH/C-O-C bonds	286.32(ii)	1.36	10.05
		C=O/O=C-O bonds	288.15(iii)	1.35	27.00
$Cu_xCo_yO_z$ + 1.5wt%GO	Cu2*p3/2*	Metal Cu^{+} ions (Cu_2O bonds)	932.30(i)	1.70	68.08
		Metal Cu^{2+} ions (CuO bonds)	934.25(ii)	2.20	31.92
	Co2*p3/2*	Co_3O_4	779.07(i)	2.08	30.65
		Co_2O_3	780.73(ii)	3.30	33.33
	Co2*p3/2* sat.	Co_3O_4/Co_2O_3	785.64(iii)	5.99	36.02
	O1*s*	Metal oxides (Cu/Co oxides)	529.03(i)	1.08	80.16
		Metal oxides (Cu/Co oxides)	529.45(ii)	1.37	9.65
		Surface oxygen/C=O/O=C-O bonds	530.98(iii)	1.35	10.19
	C1*s*	C-C/C-H bonds	284.60(i)	1.37	77.68
		C-OH/C-O-C bonds	286.55(ii)	1.35	15.17
		C=O/O=C-O bonds	288.81(iii)	1.34	7.14

Note: (i) – (iii) notations in the BE column indicate the component parts of deconvoluted high resolution XPS spectra of Figs. 2-5.

Table 5. Energy band-gaps of $Cu_xCo_yO_z$ thin film coatings with the addition of graphene oxide.

Coatings name	Band-gap, E_g (eV)
$Cu_xCo_yO_z$	2.4
$Cu_xCo_yO_z$ + 0.1wt% GO	2.2
$Cu_xCo_yO_z$ + 0.5wt% GO	2.1
$Cu_xCo_yO_z$ + 1wt% GO	1.7
$Cu_xCo_yO_z$ + 1.5wt% GO	1.6

Table 6. Optical properties of the $Cu_xCo_yO_z$ thin film coatings with the addition of graphene oxide.

Sample compositions	Absorptance, α (%)	Emittance, ε (%)	Selectivity, $s = \alpha/\varepsilon$
$Cu_xCo_yO_z$	83.40	5.70	14.63
$Cu_xCo_yO_z$ + 0.1wt% GO	84.00	5.27	15.85
$Cu_xCo_yO_z$ + 0.5wt% GO	84.30	4.80	17.56
$Cu_xCo_yO_z$ + 1wt% GO	85.60	3.20	26.75
$Cu_xCo_yO_z$ + 1.5wt% GO	86.14	2.97	29.01

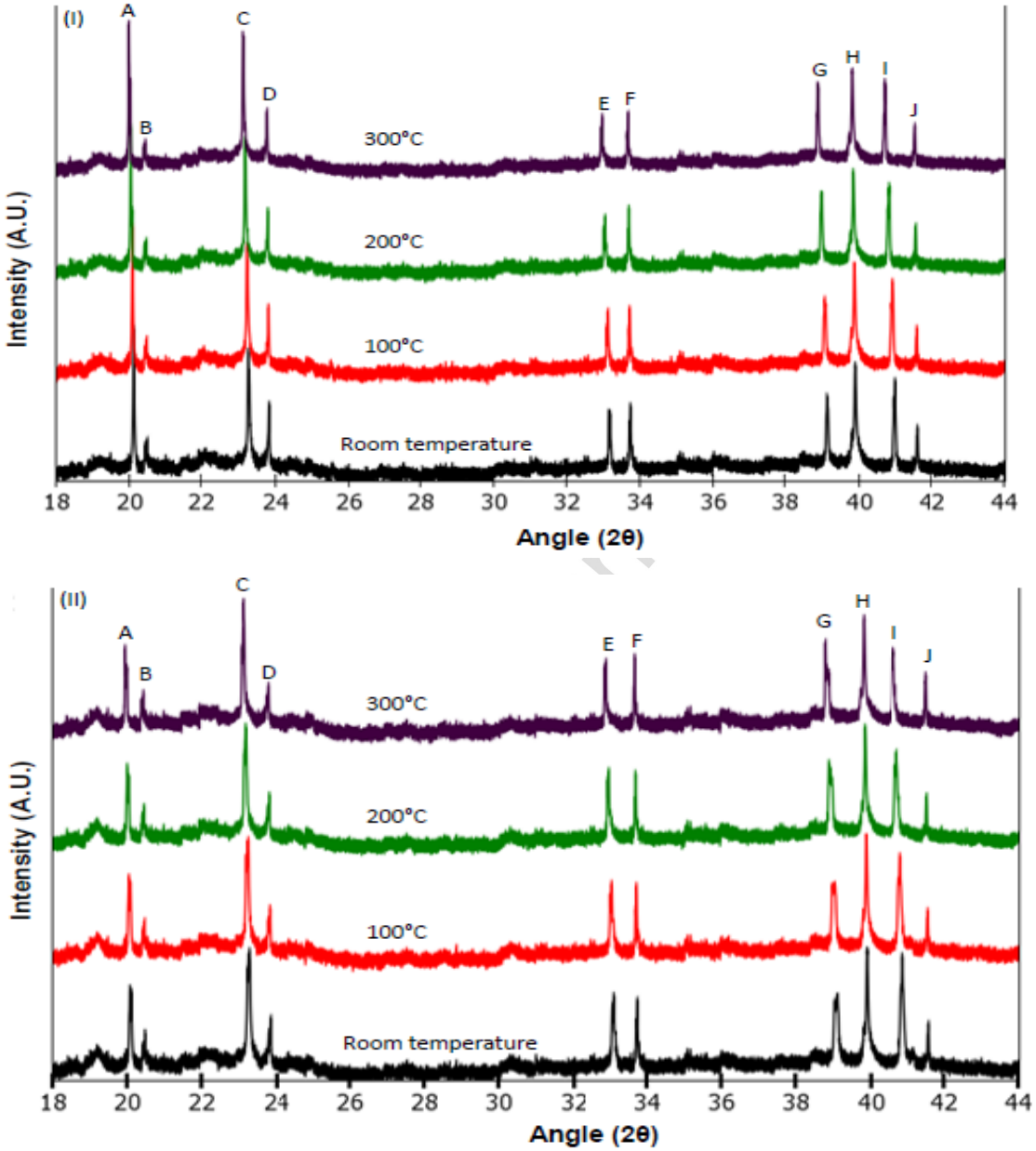

Fig. 1. Synchrotron radiation X-ray diffraction data of (A) $Cu_xCo_yO_z$ coatings, and (B) $Cu_xCo_yO_z$ thin film coatings with 1.5 wt% of graphene oxide at room temperature, 100 °C, 200 °C, and 300 °C acquired at the powder diffraction beamline at Australian Synchrotron, Melbourne.

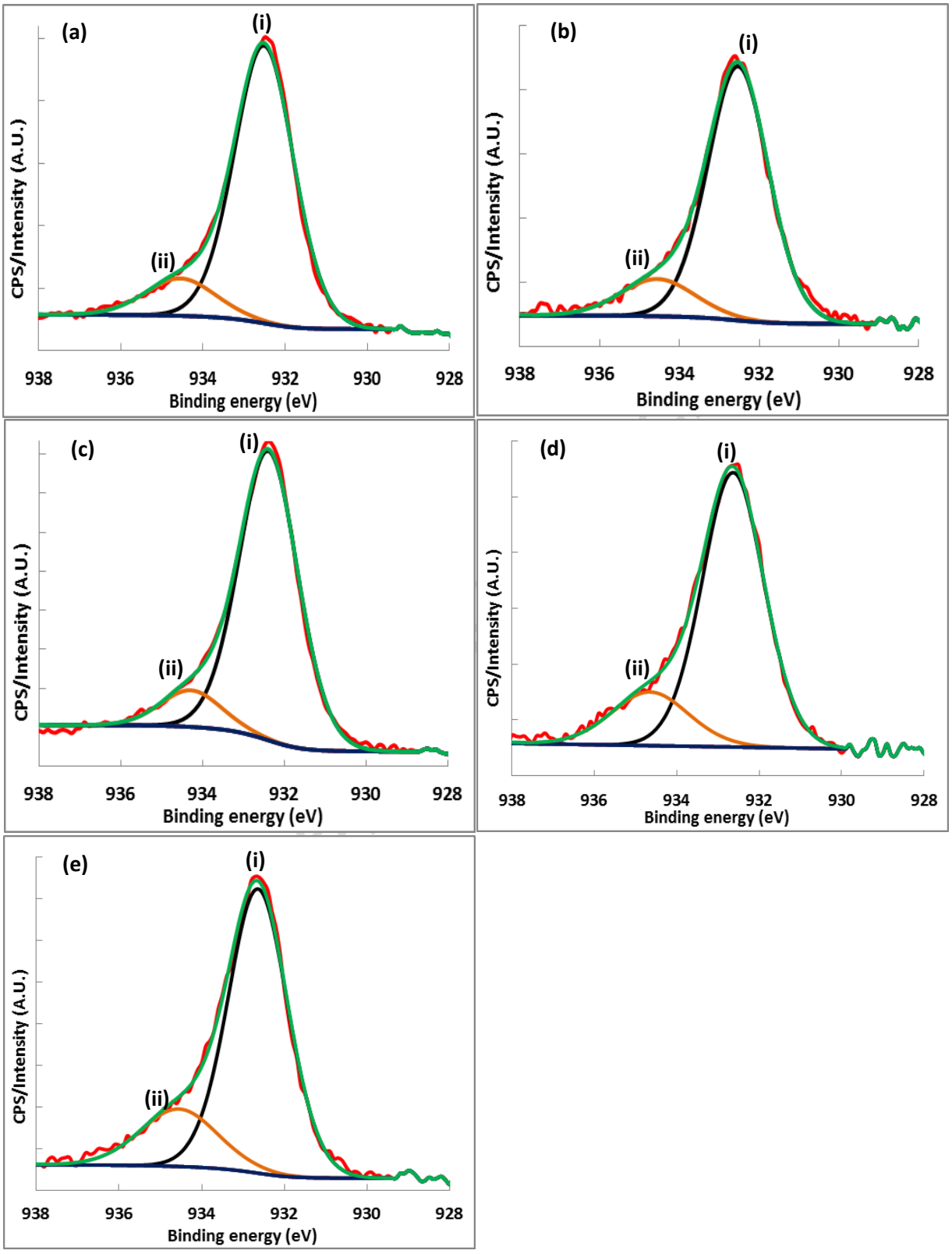

Fig. 2. Decoupling of XPS spectra of Cu2$p_{3/2}$ peak of CuCoO thin film coatings: (a) $Cu_xCo_yO_z$ (b) $Cu_xCo_yO_z$ + 0.1wt.% GO, (c) $Cu_xCo_yO_z$ + 0.5wt.% GO, (d) $Cu_xCo_yO_z$ + 1wt.% GO, (e) $Cu_xCo_yO_z$ + 1.5wt.% GO.

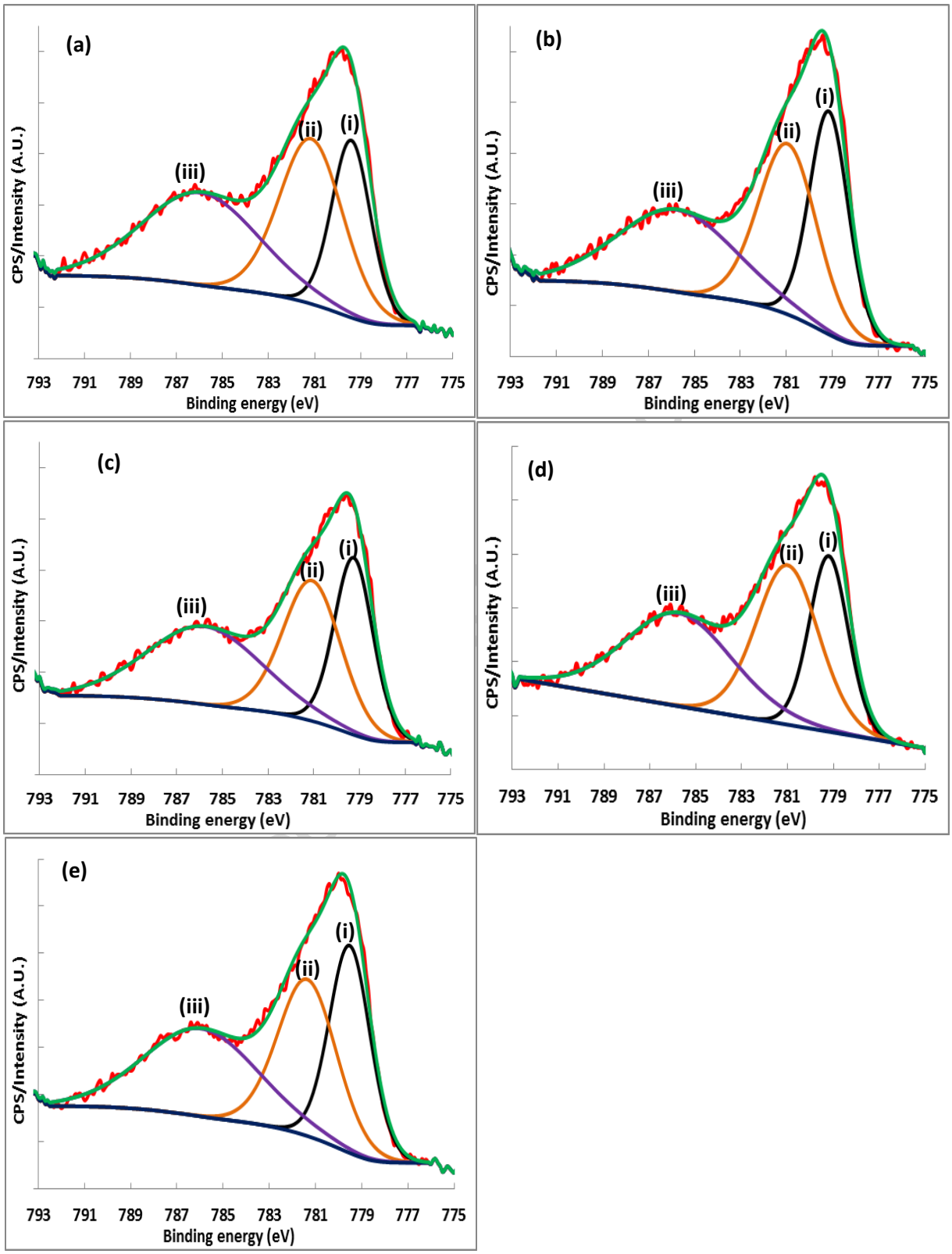

Fig. 3. Decoupling of XPS spectra of Co2$p_{3/2}$ peak of CuCoO thin film coatings: (a) $Cu_xCo_yO_z$ (b) $Cu_xCo_yO_z$ + 0.1wt% GO (c) $Cu_xCo_yO_z$ + 0.5wt% GO (d) $Cu_xCo_yO_z$ + 1wt% GO (e) $Cu_xCo_yO_z$ + 1.5wt% GO.

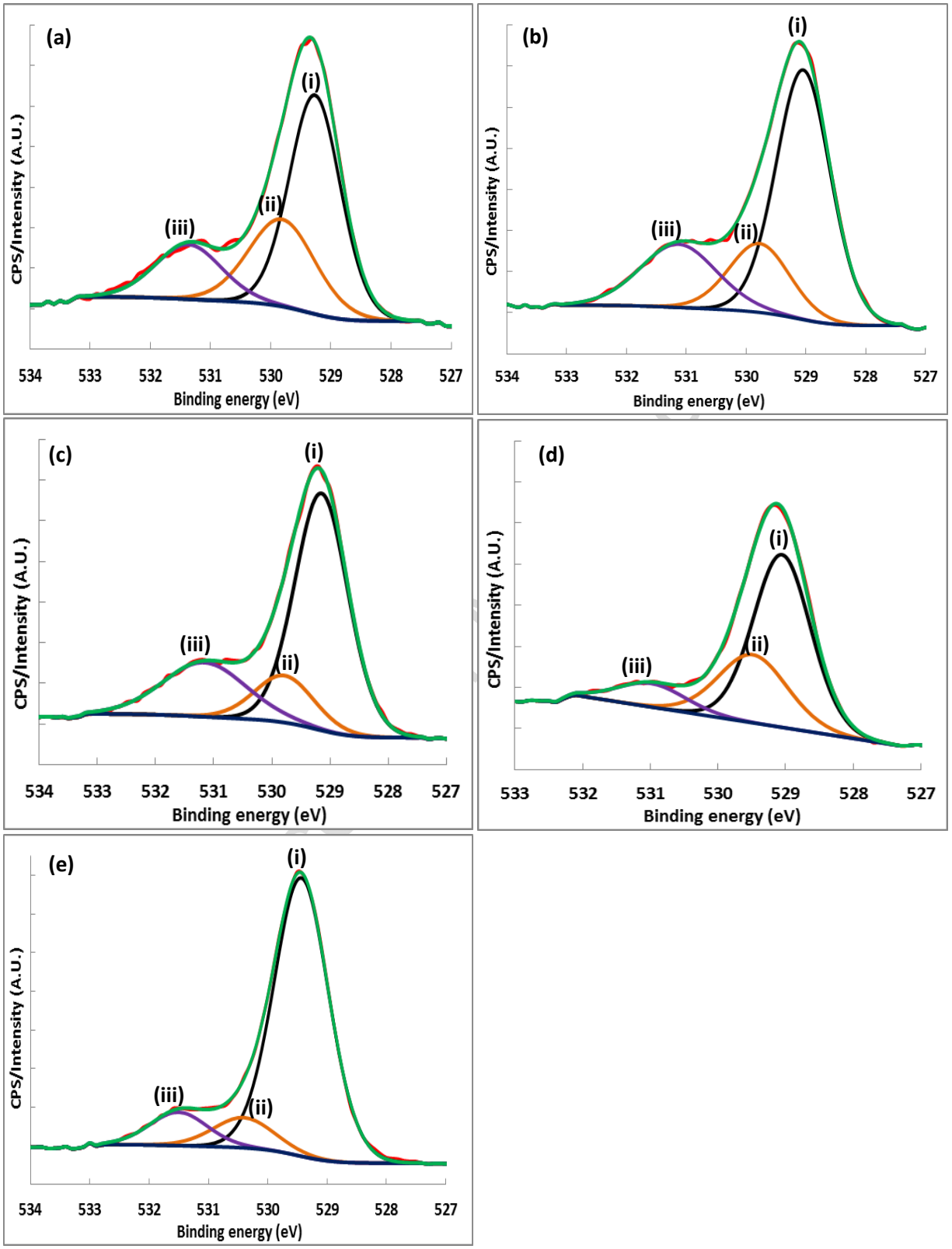

Fig. 4. Decoupling of XPS spectra of O*1s* peak of CuCoO thin film coatings: (a) $Cu_xCo_yO_z$ (b) $Cu_xCo_yO_z$ + 0.1wt% GO (c) $Cu_xCo_yO_z$ + 0.5wt% GO (d) $Cu_xCo_yO_z$ + 1wt% GO (e) $Cu_xCo_yO_z$ + 1.5wt% GO.

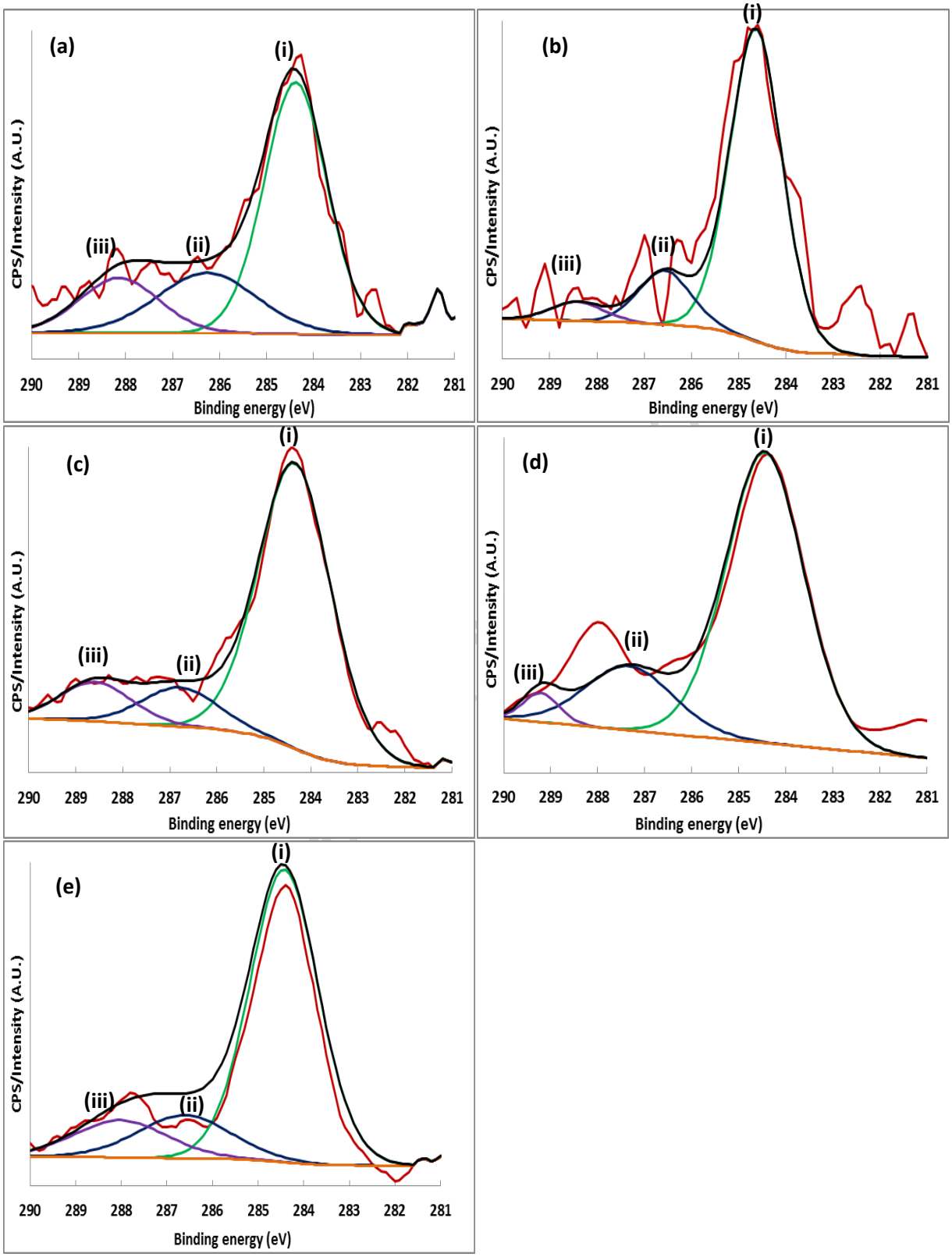

Fig. 5. Decoupling of XPS spectra of C1*s* peak of CuCoO thin film coatings: (a) $Cu_xCo_yO_z$ (b) $Cu_xCo_yO_z$ + 0.1wt% GO (c) $Cu_xCo_yO_z$ + 0.5wt% GO (d) $Cu_xCo_yO_z$ + 1wt% GO (e) $Cu_xCo_yO_z$ + 1.5wt% GO.

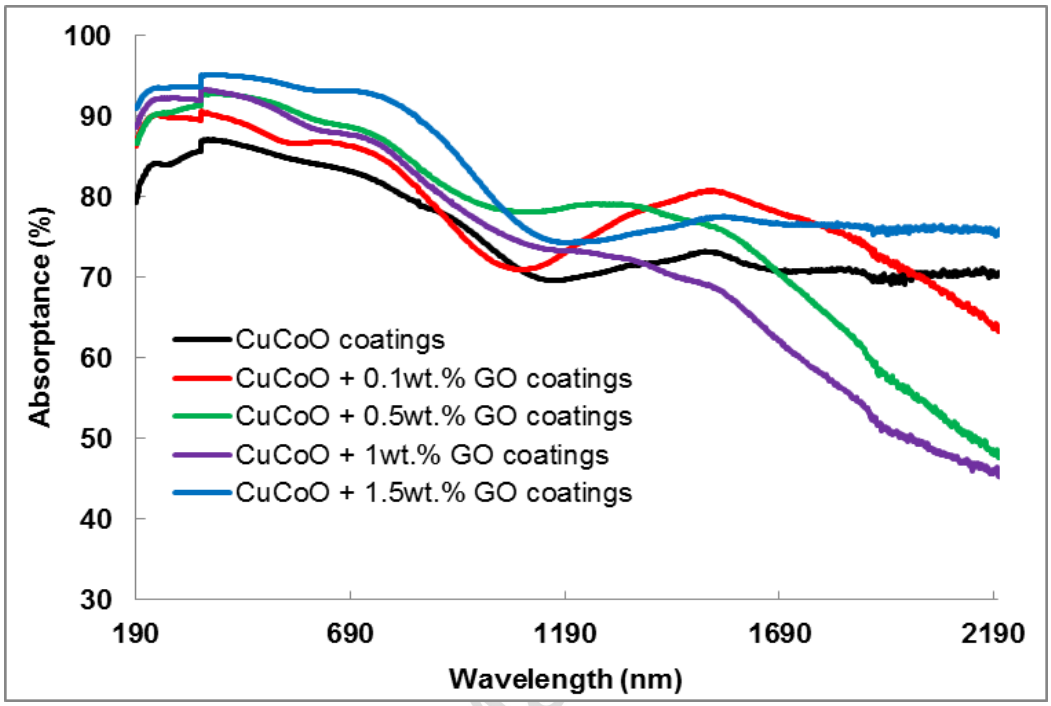

Fig. 6. UV-Vis absorptance spectra of sol-gel $Cu_xCo_yO_z$ thin film coatings without and with the addition of graphene oxide.

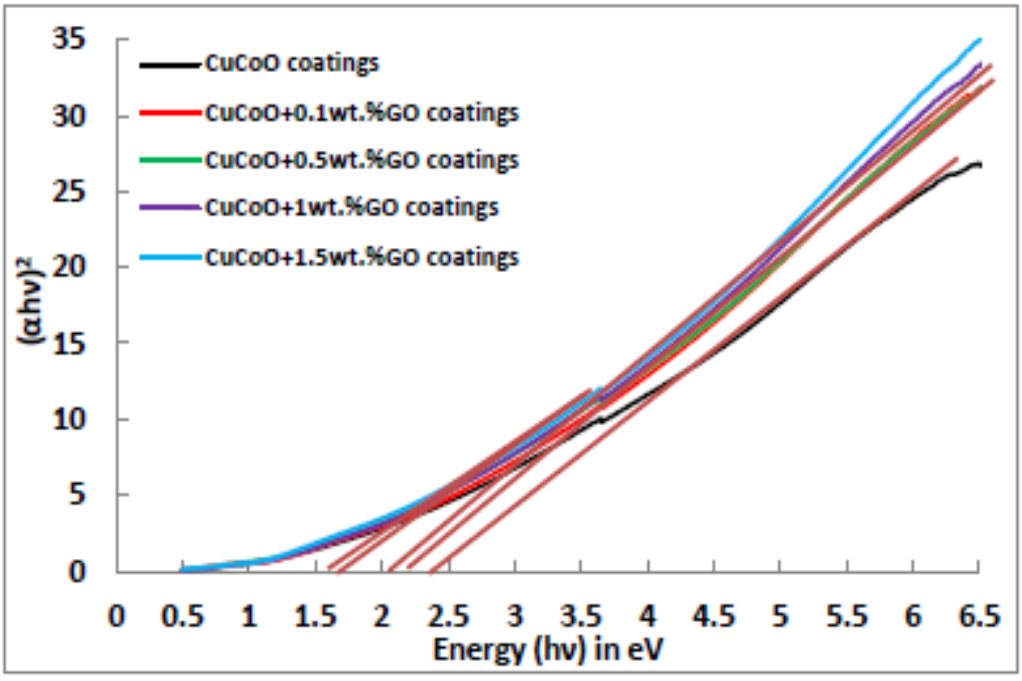

Fig. 7. Estimation of energy band-gaps of sol-gel derived $Cu_xCo_yO_z$ thin film coatings without and with the addition of graphene oxide.

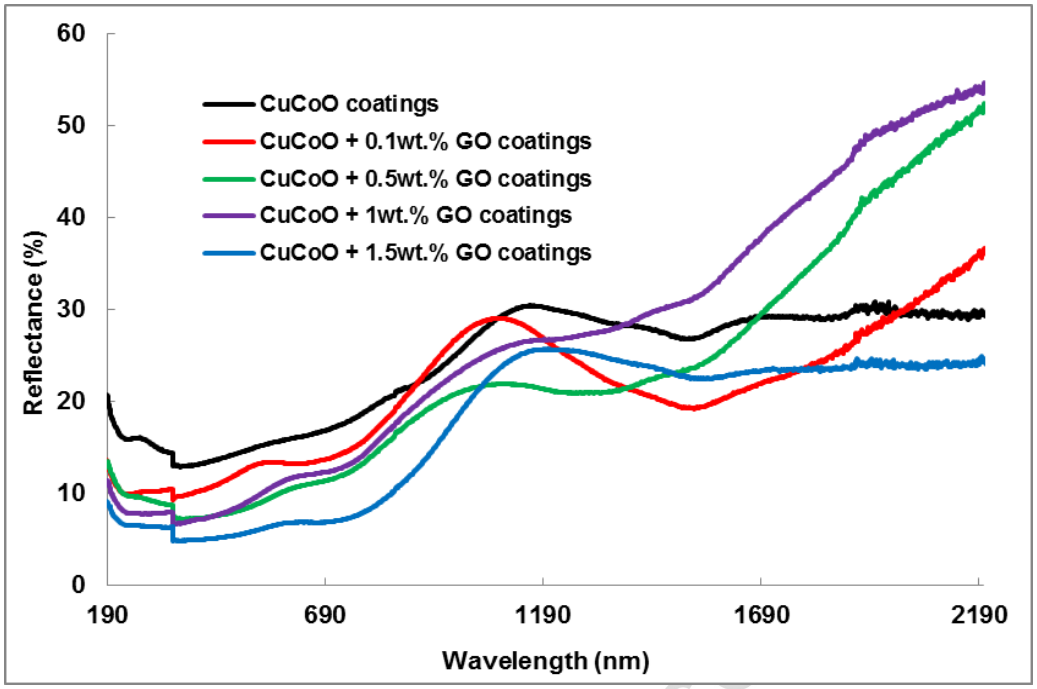

Fig. 8. UV-visible reflectance spectra of $Cu_xCo_yO_z$ thin film coatings without and with the addition of graphene oxide.

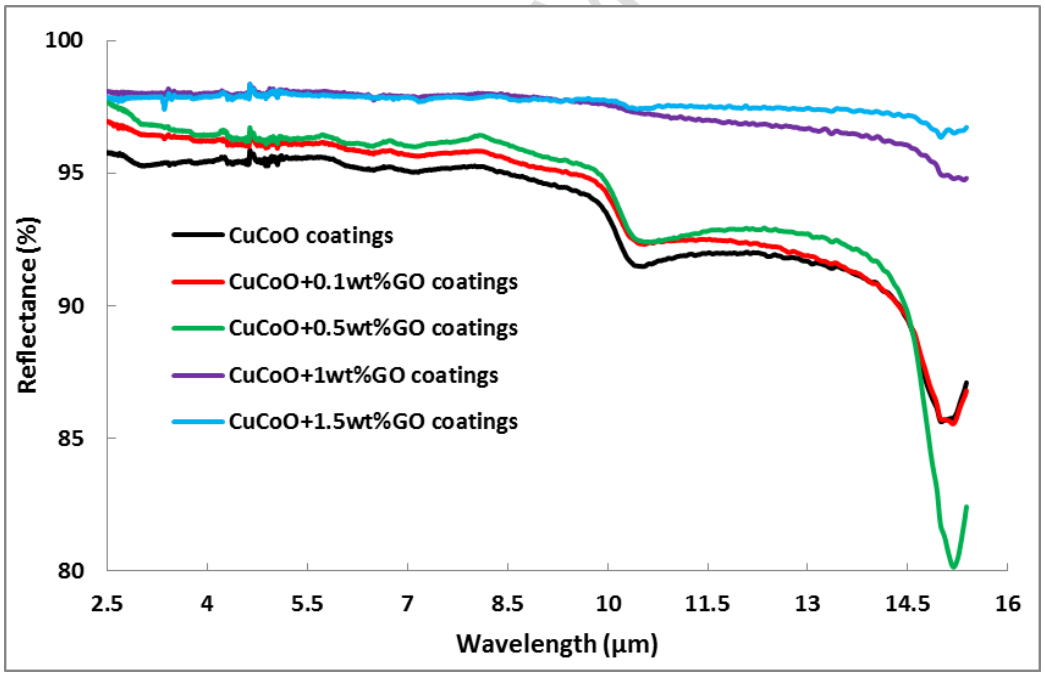

Fig. 9. FTIR reflectance spectra of sol-gel derived $Cu_xCo_yO_z$ coatings without and with the addition of graphene oxide.